JOURNAL OF GEOPHYSICAL RESEARCH, VOL. 89, NO. B13, PAGES 11,401–11,413, DECEMBER 10, 1984

# Thermomechanical Evolution of Oceanic Fracture Zones

DAVID T. SANDWELL

*National Geodetic Survey, Charting and Geodetic Services, National Ocean Service, National Oceanic and Atmospheric Administration, Rockville, Maryland*

A fracture zone (FZ) model is constructed from existing models of the thermal and mechanical evolution of the oceanic lithosphere. As the lithosphere cools by conduction, thermal and mechanical boundary layers develop and increase in thickness as $(age)^{1/2}$. Surface expressions of this development, such as topography and deflection of the vertical (i.e., gravity field), are most apparent along major FZ's because of the sharp age contrast. A simple model, including the effects of lateral heat transport but with no elastic layer, predicts that variations in seafloor depth and deflection of the vertical will become increasingly smooth and ultimately disappear as the FZ ages. Observations, however, show that both the FZ topography and the deflection of the vertical remain sharp as the FZ evolves. These two observations, as well as the observed asymmetry in deflection of the vertical profiles across the Udintsev, Romanche, and Mendocino FZ's, are explained by including a continuous elastic layer in the model. The asymmetry in deflection of the vertical is a consequence of elastic thickness variations across the FZ. Modeling also shows that the evolution of the FZ topography is extremely sensitive to the initial thermal structure near the ridge-transform intersection. Model geoid steps and their development with age are used to access techniques for measuring geoid offsets across FZ's. Reasonable step estimation techniques will underestimate the overall step amplitude by up to 50%. This implies that abnormally thin thermal boundary layers, derived from studies of geoid height versus age, are not required by the data.

## INTRODUCTION

Fracture zones are linear scars in the seafloor produced by transform faulting [*Wilson*, 1965]. Topography along their inactive segments consists of long ridges, troughs, and scarps which separate regions of different depth [*Menard and Atwater*, 1969]. In spite of erosion and sedimentation, fracture zone (FZ) topography does not diminish and become smoother with age; instead it intensifies and becomes more rugged with age. This persistence indicates that vertical tectonic movements remain after the FZ migrates beyond the active transform fault. As shown below, and in a previous paper [*Sandwell and Schubert*, 1982*b*], the vertical motions, resulting in ridge and trough tropography, are due to thermomechanical interactions in the lithosphere. These are driven by the age contrast across the FZ.

In addition to their characteristic ridge and trough topographies, FZ's are also associated with linear steplike geoid undulations [*Crough*, 1979; *Detrick*, 1981; *Sandwell and Schubert*, 1982*a*; *Cazenave et al.*, 1982]. Recent advances in measuring geoid undulations by satellite altimetry [*Stanley*, 1979; *Born et al.*, 1979] have yielded detailed geoid maps over most ocean areas (William F. Haxby, personal communication, 1983; *Sandwell* [1984]). Besides the ocean trenches, these maps are dominated by steplike FZ signals which persist on even the oldest seafloor. Since FZ's reveal past transform fault orientations, they will provide constraints on plate reconstruction models in the remote southern ocean basins where bathymetric data are sparse.

To explain both the topographic and gravitational signals of FZ's, a realistic model is developed and compared with Seasat altimeter data across three major FZ's. The model is based upon existing thermal and mechanical models of the oceanic lithosphere. These are the following: (1) the thermal model—After lithosphere is created at a spreading ridge, it cools by conduction [*Turcotte and Oxburgh*, 1967]. This boundary layer cooling model predicts an error function geotherm, which is a good approximation to the actual geotherm, for seafloor ages less than 70 Ma [*Parsons and Sclater*, 1977]; (2) the subsidence model—Lithospheric cooling is accompanied by thermal contraction. Because the asthenosphere has fluidlike properties over million-year time scales, the thermally induced density increases are compensated by subsidence proportional to $(age)^{1/2}$ [*Parker and Oldenburg*, 1973]; (3) the mechanical model—As the upper portion of the lithosphere cools, an elastic layer develops and grows in thickness as $(age)^{1/2}$ [*Watts*, 1978; *Caldwell and Turcotte*, 1979].

These three factors depend upon the age of the lithosphere so they will vary abruptly across a FZ because of the sharp age contrast there. The model developed below also includes the effect of lateral heat conduction, which tends to smooth the variations in the thermal [*Louden and Forsyth*, 1976] and mechanical structure. It is similar to the model used by *Sandwell and Schubert* [1982*b*] to explain the ridges and troughs along Pacific FZ's. However, due to a newly developed technique for solving the flexure problem with spatially variable rigidity (see appendix), this new model is more realistic than our earlier model. It can also accommodate a variety of initial conditions which, as shown below, have a major influence upon the evolution of FZ topography.

In addition to calculating FZ topography this new model is used to calculate the evolution of the geoid signature across a FZ. Model profiles are then compared with Seasat profiles across the Udintsev FZ in the South Pacific, the Romanche FZ in the Equatorial Atlantic, and the Mendocino FZ in the North Pacific. The model including lithospheric flexure explains the persistence of sharp FZ geoid steps on old seafloor as well as the asymmetry of the geoid steps across major FZ's. Since the model is based upon half-space cooling, it does not explain the disappearance of the thermal part of the FZ geoid signature.

After showing good agreements between model predictions and Seasat altimeter profiles across major FZ's, the model profiles are used to access the various techniques for estimating the overall geoid offsets across FZ's. *Detrick* [1981], using a simple FZ model, showed that reasonable step estimation techniques will underestimate overall offsets by as



Paper number 4B1125.

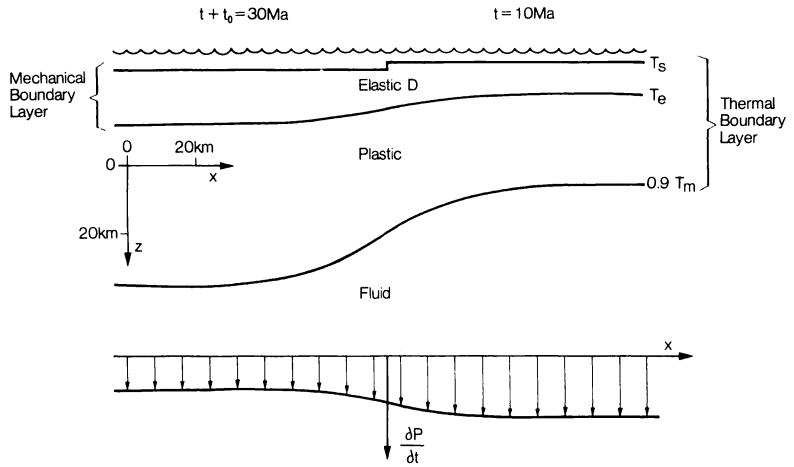


Fig. 1. Thermomechanical fracture zone model (drawn to scale). Thermal and mechanical boundary layers develop and increase in thickness as the lithosphere cools. The upper portion of the lithosphere, between the seafloor ($T_s$) and the stress relaxation isotherm ($T_e$), is elastic while the lower portion, between $T_e$ and 0.9 $T_m$ (mantle temperature), is plastic. Beneath the thermal boundary layer the rocks are fluid. The age contrast across the FZ (20 Ma) and lateral heat conduction result in continuous transition in thermal and mechanical properties. The younger lithosphere cools and contracts faster than the older lithosphere producing lateral variations in thermal buoyancy force ($\partial P/\partial t$).

much as 25%. A similar analysis using this new model shows that steps may be underestimated by as much as 50%. These model predictions, if correct, will force reinterpretation of published geoid height versus age data derived from altimeter profiles across FZ's.

## Model

Figure 1 shows a simplified model of the oceanic lithosphere. It consists of both thermal and mechanical boundary layers which increase in thickness as the lithosphere ages and cools. The base of the elastic layer is defined by the stress relaxation temperature $T_e$ of approximately 450° [*Watts et al.*, 1980] (definitions and values for all parameters are given in Table 1) and is characterized by a flexural rigidity $D$ which is proportional to the elastic thickness cubed. For mathematical convenience this elastic layer is approximated by a thin elastic plate. A plastic layer lies between the elastic layer and the fluid mantle. It cannot support the large flexural stresses but is rigid enough to prohibit large-scale flow that would smooth the thermal transition. The base of the thermal boundary layer is defined by a fraction of the deep mantle temperature $T_m$ of 1365°C. The seawater temperature $T_s$ ($\sim$0°C) constrains the temperature of the upper surface of the lithosphere. Both the thermal and mechanical boundary layers vary in thickness across a FZ because of the age contrast $t_0$. It is assumed that thermal and mechanical variations are two dimensional.

Initially (i.e., $t = 0$), the geotherm on the left side of the FZ (Figure 1) corresponds to an age of $t_0$, while the right side has a constant temperature of $T_m$. Thus, initially, the elastic thickness of the right side is zero. There is also an initial sharp step in seafloor depth across the FZ. Later on these idealized initial conditions are relaxed slightly to determine the sensitivity of FZ evolution to the initial conditions.

The model represents the development of the FZ outside of the active transform fault. Along this seismically inactive segment it is assumed that there there are no significant horizontal motions. Based upon the results of our previous study of bathymetry across FZ's in the North Pacific [*Sandwell and Schubert*, 1982*b*], it is also assumed that vertical slip does not occur along the FZ. As it evolves from its initial state (see Figure 1) the lithosphere on the right (younger) side cools more rapidly than the lithosphere on the left (older) side, although these spatial variations are smoothed somewhat by lateral heat conduction. Thermal contraction produces a downward pressure which is stronger on the right side than on the left side, as shown in the lower part of Figure 1. Stresses produced by differential contraction in the region of strong lateral temperature gradient are relieved by strain in the plastic layer and are not large enough to cause failure in the elastic layer. As the FZ ages, the elastic layer on the right side develops rapidly to form a continuous elastic layer. The lateral pressure variations flex the elastic layer. The shape of the flexure depends upon the elastic thickness variations. Thus the thermal evolution of the FZ both drives the flexure and modulates the elastic thickness.

## Temperature

The two-dimensional thermal structure near a FZ is found by solving the time-dependent heat conduction equation

$$\frac{\partial^2 T}{\partial x^2} + \frac{\partial^2 T}{\partial z^2} = \frac{1}{\kappa}\frac{\partial T}{\partial t} \tag{1}$$

where $\kappa$ is the thermal diffusivity. The initial temperature distribution is

$$T(x, z, t_0) = \begin{cases} T_s + (T_m - T_s)\,\mathrm{erf}\left(\dfrac{z}{2\sqrt{\kappa t_0}}\right) & x < 0 \\ T_m & x > 0 \end{cases} \tag{2}$$

The surface boundary condition is

$$T(x, 0, t) = T_s \tag{3}$$

*Carslaw and Jaeger* [1959, p. 276] expressed the solution to this problem as a two-dimensional convolution of the initial temperature distribution with a line source Green's function. For the initial temperature distribution given in (2) the convolution integral can be evaluated analytically [*Sandwell and Schubert*, 1982*b*] and is

$$T(x, z, t) = T_s + \frac{(T_m - T_s)}{2}\left[\mathrm{erfc}\left(\frac{x}{2\sqrt{\kappa(t - t_0)}}\right)\mathrm{erf}\left(\frac{z}{2\sqrt{\kappa t}}\right) + \mathrm{erfc}\left(\frac{-x}{2\sqrt{\kappa(t - t_0)}}\right)\mathrm{erf}\left(\frac{z}{2\sqrt{\kappa(t - t_0)}}\right)\right] \tag{4}$$

The function erfc ($x$) ranges from 2 to 0 as $x$ goes from $-\infty$ to $\infty$. Thus far from the FZ the geotherm follows the error function of the boundary layer convection model [*Turcotte and Oxburgh*, 1967]. Because of lateral heat conduction, temperatures vary continuously across a FZ [*Louden and Forsyth*, 1976].

## Density, Depth, and Pressure

Variations in density are coupled to temperature variations because of thermal expansion. The following equation of state is used

$$\rho(x, z, t) = \rho_m[1 - \alpha(T(x, z, t) - T_m)] \tag{5}$$

where $\rho_m$ is the density of the mantle at temperature $T_m$, $\alpha$ is the thermal expansion coefficient, and $z$ is depth measured from the seafloor.

If the lithosphere is in local isostatic equilibrium, then the integral of density over depth must remain constant as the FZ evolves. This compensation is achieved by space and time variations in seafloor depth $d(x, t)$ given by

$$d(x, t) = d_{\text{ref}} + \frac{\alpha\rho_m}{(\rho_m - \rho_w)} \int_0^\infty (T_m - T(x, z, t))\, dz \tag{6}$$

where $\rho_w$ is seawater density and $d_{\text{ref}}$ is the seafloor depth at the spreading ridge. The analytic expression for $d$ is obtained by integrating (6) using (4). The result is

$$d(x, t) = d_{\text{ref}} + \frac{\alpha\rho_m(T_m - T_s)}{(\rho_m - \rho_w)} \sqrt{\frac{\kappa}{\pi}} \left[ \sqrt{t - t_0} + \sqrt{t} + \text{erf}\left(\frac{x}{2\sqrt{\kappa(t - t_0)}}\right)(\sqrt{t - t_0} - \sqrt{t}) \right] \tag{7}$$

If seafloor depth does not change to compensate the density increases, then pressure will build up with increasing time as

$$P(x, t) = \alpha\bar{g}\rho_m(T_m - T_s) \sqrt{\frac{\kappa}{\pi}} \left[ \sqrt{t - t_0} + \sqrt{t} + \text{erf}\left(\frac{x}{2\sqrt{\kappa(t - t_0)}}\right)(\sqrt{t - t_0} + \sqrt{t}) \right] \tag{8}$$

where $\bar{g}$ is the average acceleration of gravity. When lithosphere strength is included in the model, this pressure term drives the lithosphere flexure.

Figure 2 shows the evolution of FZ topography, assuming local isostatic equilibrium (i.e., equation (7)). An age offset $t_0$ of 20 Ma was used in this and subsequent calculations. Depth curves are labeled according to the age of the younger (right) lithospheric segment. Initially, the step is sharp; however, in just a few million years, lateral heat conduction smooths the step.

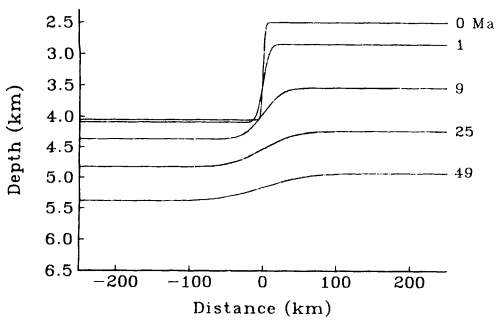


Fig. 2. Variations in seafloor depth for the FZ model with no elastic layer. The age offset is 20 Ma and ages of the younger lithosphere (right) are 0, 1, 9, 25, and 49 Ma. Lateral heat conduction and local isostasy are responsible for the pronounced smoothing of the FZ step with age.

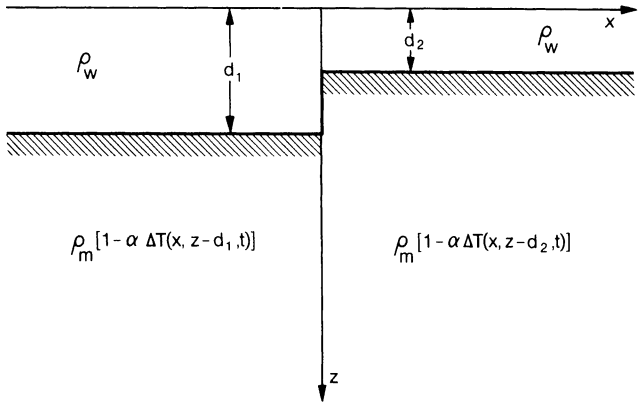


Fig. 3. Density structure used for calculating variations in gravitational potential. The seawater density is $\rho_w$ and the lithosphere density is $\rho_m$ plus a small temperature-dependent term ($-\alpha\rho_m\Delta T$).

## Gravitational Potential

Variations in gravitational potential expressed as gravity anomalies, deflections of the vertical, or geoid heights can also be calculated from this model. A flat-earth, two-dimensional approximation is used, and the lithosphere is assumed to be in local isostatic equilibrium. The regional effects caused by flexure are included later. Variations in potential are found by convolving the density structure shown in Figure 3 with the ln ($r$) Green's function. In Figure 3, $\Delta T$ is $T - T_m$ and $d_1$, $d_2$ are the depths on the left and right side of the FZ, respectively. Figure 3 shows a sharp step in the seafloor, whereas the actual step for this model is smooth as shown in Figure 2. Potential variations corresponding to these depth differences are included as a separate term. Before integrating, a constant density is subtracted from each of three layers, and step functions are used to account for the step in the thermal structure. The resulting density variations $\Delta\rho$ are

$$\Delta\rho(x, z, t) = \begin{cases} 0 & z < d_2 \\ \rho_w - \rho_m(1 + \alpha T_m)(1 - H(x)) & \\ \quad - \alpha\rho_m T(z - d_2)H(x) & d_2 < z < d_1 \\ -\alpha\rho_m T(z - d_1)(1 - H(x)) & \\ \quad - \alpha\rho_m T(z - d_2)H(x) & d_1 < z \end{cases} \tag{9}$$

where $H(x)$ is the unit step function. The $x$ convolution integral cannot be evaluated analytically because the density structure is so complicated. However, in the wave number domain, where $\Delta\hat{\rho}$ is the Fourier transform of $\Delta\rho$ given by

$$\Delta\hat{\rho}(k, z, t) = \int_{-\infty}^{\infty} \Delta\rho(x, z, t)e^{-ikx}\, dx \tag{10}$$

and the inverse transform of $\Delta\hat{\rho}$ is

$$\Delta\rho(x, z, t) = \frac{1}{2\pi} \int_{-\infty}^{\infty} \Delta\hat{\rho}(k, z, t)e^{ikx}\, d\kappa \tag{11}$$

the $x$ convolution becomes a muliplication. Also in this

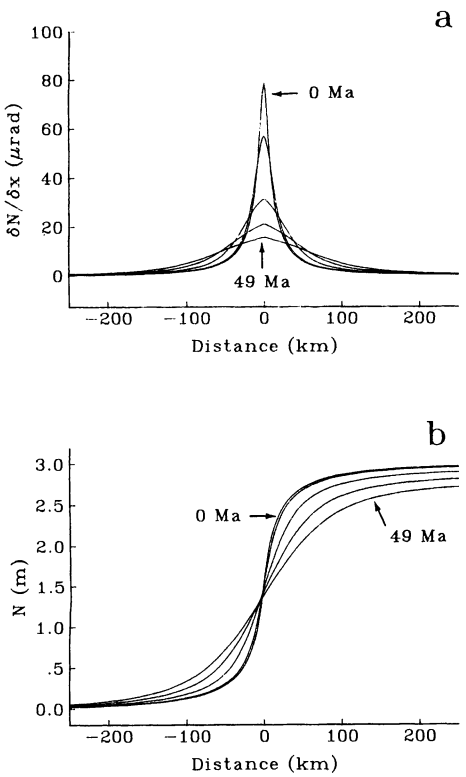


Fig. 4. (*a*) Deflection of the vertical and (*b*) geoid height across a FZ with a 20-Ma age offset. The model and ages are the same as Figure 2. Lateral heat conduction and local isostasy cause the initial sharp peak in deflection of the vertical to decay rapidly. The overall amplitude of the geoid step remains constant with age.

domain, the $z$ convolution integral for the potential, evaluated at $z = 0$, is the Laplace transform of the density structure

$$\hat{U}(k, t) = \frac{2\pi G}{|k|} \int_0^\infty \Delta\hat{\rho}(k, z, t) e^{-|k|z}\, dz \tag{12}$$

where $G$ is the gravitational constant. Both the Fourier transform integral (10) and the Laplace transform integral (12) can be evaluated analytically for the density structure described by equation (9). Tables of Fourier and Laplace transforms, such as the CRC Standard Mathematical Tables [*Beyer*, 1976], were used to evaluate several of the integrals. After the integrations, the Fourier transform of the potential is

$$\begin{aligned}\hat{U}(\kappa, t) = \frac{2\pi i G}{k^3} \{&[\rho_m - \rho_w + \alpha\rho_m(T_m - T_s)](e^{-|k|d_1} - e^{-|k|d_2}) \\ &+ \alpha\rho_m \frac{(T_m - T_s)}{2} e^{-|k|d_2} \\ &\cdot [s^+(k, t)b(|k|\sqrt{\kappa(t - t_0)}) + s^-(k, t)b(|k|\sqrt{\kappa t})] \\ &- \alpha\rho_m \frac{(T_m - T_s)}{2} e^{-|k|d_1} \\ &\cdot [s^-(k, t)b(|k|\sqrt{\kappa(t - t_0)}) + s^+(k, t)b(|k|\sqrt{\kappa t})]\end{aligned} \tag{13}$$

where $b(z) = e^{z^2}\,\mathrm{erfc}\,(z)$. The functions $s^+$ and $s^-$ incorporate the effects of lateral heat conduction, where

$$s^+(k, t) = 1 + \exp\,[-k^2\kappa(t - t_0)] \tag{14}$$

and

$$s^-(k, t) = 1 - \exp\,[-k^2\kappa(t - t_0)] \tag{15}$$

The time interval $t - t_0$ corresponds to the thermal contact time across an FZ. If $t - t_0$ is replaced by zero in $s^+$ and $s^-$, then $s^+ = 2$ and $s^- = 0$, and the model reduces to the thermogravitational edge effect model, which does not include lateral heat conduction.

As stated above, an additional term must be added to (13) to account for the smoothness of the FZ topography. The difference between the smooth step given in (7) and the step function used in (9) is

$$w(x, t) = \frac{2\alpha\rho_m(T_m - T_s)}{(\rho_m - \rho_w)} \sqrt{\frac{\kappa}{\pi}} \cdot \left[H(x) - \tfrac{1}{2}\,\mathrm{erfc}\left(\frac{x}{2\sqrt{\kappa(t - t_0)}}\right)\left(\sqrt{t} - \sqrt{t - t_0}\right)\right] \tag{16}$$

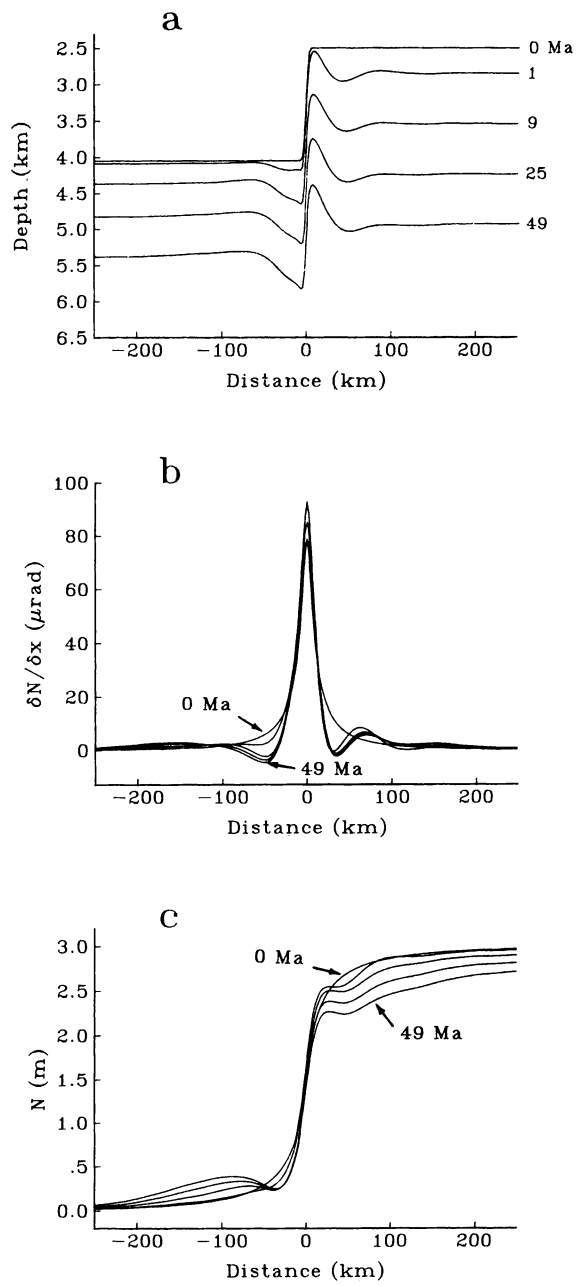


Fig. 5. Evolution of an FZ (20-Ma age offset), which includes the mechanical boundary layer: (*a*) The elastic layer prohibits decay of the initial FZ scarp (0 Ma). Within a few million years an asymmetric ridge and trough develop. (*b*) The deflection of the vertical peak retains its high initial value, reflecting the persistence of the bathymetric scarp. Asymmetric side lobes develop as the FZ ages. (*c*) The geoid step changes in shape but not in amplitude as the FZ evolves.

The approximate (i.e., using only the first term in *Parker*'s [1972] expansion) potential $\hat{U}_T(k)$ produced by this extra topography can also be calculated analytically in the wave number domain. It is

$$\hat{U}_T(k, t) = 4\pi i G\alpha\rho_m(T_m - T_s)\sqrt{\frac{\kappa}{\pi}}\frac{e^{-|k|d_A}}{k|k|}(\sqrt{t} - \sqrt{t - t_0}) \cdot \{1 - \exp[-k^2\kappa(t - t_0)]\} \quad (17)$$

where $d_A = (d_1 + d_2)/2$. Notice that this term vanishes when the thermal contact time $t - t_0$ goes to zero in the exponential function.

The total anomalous potential in the wave number domain is the sum of (13) and (17). The geoid height, the deflection of the vertical, and the gravity anomaly are

$$\hat{N}(k, t) = \frac{\hat{U}(k, t)}{\bar{g}} \quad (18)$$

$$\int_{-\infty}^{\infty}\frac{\partial N}{\partial x}e^{-ikx}\,dx = \frac{-ik}{\bar{g}}\hat{U}(k, t) \quad (19)$$

$$\hat{g}(k, t) = -|k|\hat{U}(k, t) \quad (20)$$

respectively. These functions are transformed back into the space domain by using the Fast Fourier Transform (FFT) algorithm.

Results are shown in Figure 4 for the evolutions of the deflection of the vertical (Figure 4*a*) and geoid height (Figure 4*b*) across a FZ with a 20-Ma age offset. Ages of the right (younger) side are 0, 1, 9, 25, and 49 Ma, corresponding to the ages shown in Figure 2. Lateral heat conduction and local isostasy are responsible for the rapid decrease, with increasing age, in the amplitude of the deflection of the vertical (Figure 4*a*). *Louden and Forsyth* [1976] showed this same effect for the gravity anomaly. The geoid height (Figure 4*b*) is obtained by integrating the deflection of the vertical in the $x$ direction. The geoid step becomes smoother as the FZ ages although its overall amplitude remains constant.

## Lithospheric Flexure

The smoothing effects predicted by this model are not observed along FZ's. Instead both the topography and geoid step remain sharp and in some cases become sharper with age. The model fails because it assumes the lithosphere has no strength and remains in local isostatic equilibrium. In this section the flexural topography is calculated and added to the model.

The differential equation describing two-dimensional flexure of a thin elastic plate with variable flexural rigidity $D(x)$ is

$$\frac{d^2}{dx^2}\left(D(x)\frac{d^2w(x)}{dx^2}\right) + \bar{g}(\rho_m - \rho_w)w(x) = P(x) \quad (21)$$

where $w$ is the topography and $P$ is the pressure exerted on the elastic plate. The flexural rigidity is related to the elastic thickness $h(x)$ by

$$D(x) = \frac{Eh^3(x)}{12(1 - \nu^2)} \quad (22)$$

where $E$ is Young's modulus, $\nu$ is Poisson's ratio, and $h$ is the depth to the $T_e$ isotherm. Both the pressure (i.e., equation (8)) and the elastic thickness are time dependent. Thus the flexural topography is also time dependent. In practice these time-dependent effects were accounted for by differentiating (21) with respect to time, solving it at discrete time steps, and finally, numerically integrating the individual flexure contributions. The differential term containing the factor $\partial D/\partial t$ was omitted because it is assumed that the elastic layer accretes from unstressed material. Time steps were chosen to increase as the square of the FZ age since pressure and rigidity change rapidly for small times.

The most difficult aspect of the flexure problem is solving (21). It could be solved by the finite difference or finite element methods. However, these techniques are difficult to apply to this FZ flexure problem because of the extremely sharp changes in flexural rigidity during the early stages of FZ evolution. A new approach to the solution of (21) is presented in the appendix. If $D(x)$ is a band-limited function, (21) can be

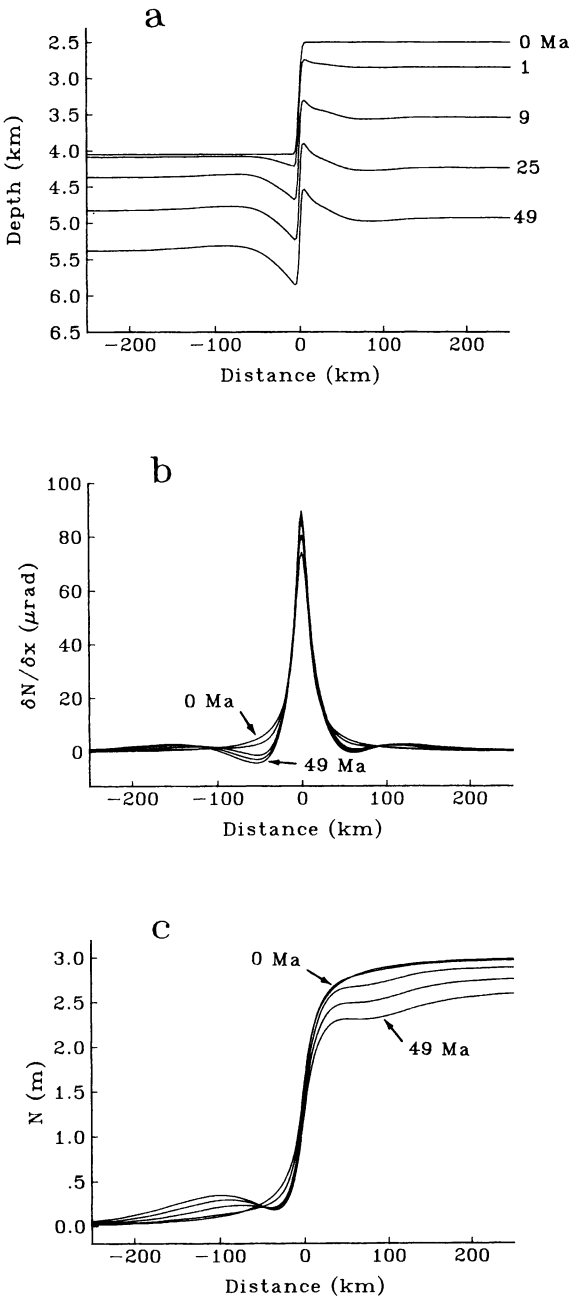


Fig. 6. Same as Figure 5, except that the initial (0 Ma) thermal transition zone is smooth rather than sharp. The transition zone width of 10 km simulates 1 Ma of lateral heat transport.

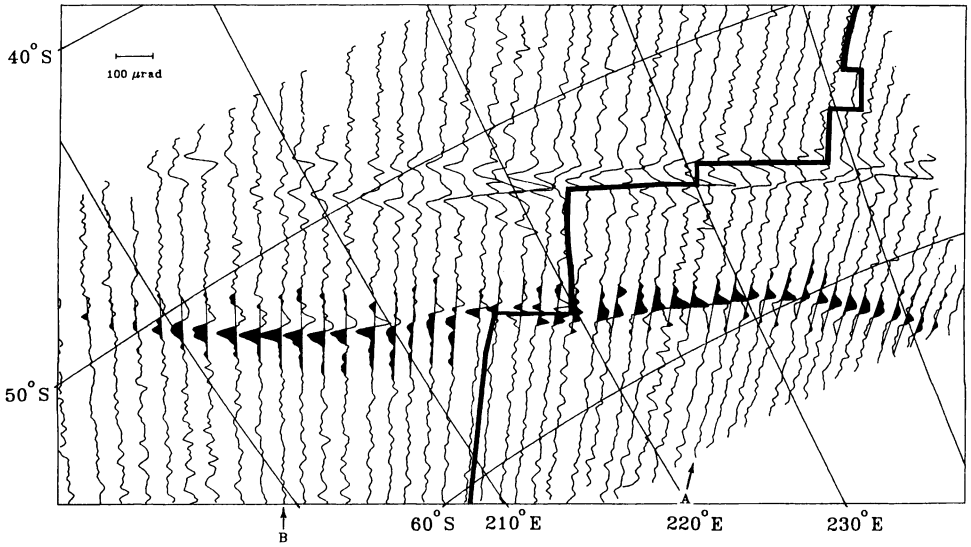


Fig. 7. Along-track deflection of the vertical profiles from differentiated Seasat altimeter passes. This subset of descending passes is plotted on an oblique Mercator projection where the pole is the relative rotation axis between the Pacific and Antarctic plates. The plate boundary (heavy line) consists of the Heezen, Tharp, and Udintsev transform faults (horizontal lines) as well as the Pacific-Antarctic Rise (vertical lines). Highlighted peaks reveal the characteristic signature of the major age-offset Udintsev FZ.

transformed into a Fredholm integral equation. It is shown that when spatial variations in rigidity are smooth (see appendix for smoothness criteria) the Fredholm equation is a linear contraction operator that can be solved, to any degree of accuracy, by iteration. Furthermore, the iteration sequence is Cauchy, and it converges uniformly in the $L_\infty$ norm. In practice, only a few iterations are required, except when rigidity variations are extreme (e.g., when the elastic layer is fractured). The major advantage of this technique is that computations are done with an FFT algorithm so that it is extremely fast.

## Results

Predictions of the complete thermomechanical model are shown in Figure 5. An age offset of 20 MA was used in this calculation. The addition of the elastic layer has a pronounced effect upon the evolution of both the topography and the deflection of the vertical. In contrast to the smooth depth variations predicted by the isostatically compensated model (Figure 2) the flexure model has a large-amplitude ridge and trough that develops in just a few million years, in agreement with *Sandwell and Schubert*'s [1982*b*] results. Moreover, the younger lithosphere flexes at a shorter wavelength than the older lithosphere because of the elastic thickness contrast across the FZ.

The difference between the models, with and without the elastic layer, is most apparent in the deflection of the vertical (Figures 5*b* and 4*a*). At zero age the two models are identical, since both are in local isostatic equilibrium. As the FZ evolves, however, the isostatically compensated FZ model predicts a decrease and ultimate disappearance of the deflection of the vertical, while for the flexure FZ model, deflections remain relatively constant. It should be noted that the overall amplitude of the geoid step (Figures 4*b* and 5*c*) does not differ between the two models. In both cases it appears that the amplitude of the geoid step decreases as the FZ evolves, but it actually remains at a constant value of 3.02 m. The implication of this apparent decrease in step amplitude for the geoid height versus age relation is discussed later.

The model incorporating the elastic layer predicts not only asymmetrical flexural topography but also an asymmetric deflection of the vertical profile (Figure 5*b*). The negative sidelobe of the older (left) side of the FZ is broader and deeper than the negative sidelobe on the younger side. In the next section these model predictions are tested by comparing them with Seasat altimeter profiles across three large age offset FZ's. Before making these comparisons, however, the sensitivity of the thermomechanical evolution of a FZ to the initial conditions is discussed.

Detailed bathymetric surveys of ridge-transform intersections (J. Fox and K. MacDonald, unpublished SEABEAM data, 1983) show that the lithosphere adjacent to the ridge crest on the older plate is anomalously shallow. This shoaling may be due to reheating and thermal expansion as the plate slides beyond the midpoint between the two spreading ridges. Thus, on the older plate, temperatures may be higher near the FZ and normal away from the FZ. On the younger plate the constant-temperature initial condition may be a good approximation, since material upwelling at the spreading ridge axis is close to its melting temperature. Recent calculations [*Forsyth and Wilson*, 1984] show that the temperature structure of a ridge-transform intersection depends primarily upon the geometry of the flow in the upwelling region.

A simple method of modifying the initial thermal structure without having to redo all of the convolution integrals is to increase the thermal contact time $(t - t_0)$. Increasing this time by an amount of $t_c$ results in a smooth initial temperature transition having a characteristic width of $2\sqrt{\kappa t_c}$. Because the base of the elastic layer follows the $T_e$ isotherm, this change also smooths the elastic thickness variation across the FZ.

The effects of modifying the initial temperature distribution are shown in Figure 6, where an initial contact time of 1 Ma was used. For this value of $t_c$ the width of the thermal transition zone is 10 km, which is consistent with *Forsyth and Wilson*'s [1984] preferred ridge-transform-ridge model. This small change has a large influence upon the shape of the flexural topography as well as the shape of the deflection of the vertical (i.e., compare Figures 5 and 6). Most of the topographic difference occurs on the young side of the FZ where

the ridge becomes sharper and the flexural wavelength becomes greater. For the deflection of the vertical the largest difference is a decrease in the amplitude of the negative sidelobe on the younger side of the FZ. This tends to enhance the asymmetry in the deflection profile. These changes occur because the initially smooth temperature transition inhibits the smoothing effects of lateral heat conduction for about 1 Ma. During this time, the elastic plate thickens, and the flexural wavelenth of the younger side becomes greater than the width of the thermal transition zone. This increase in strength suppresses further flexure at very short wavelengths.

## THE UDINTSEV FZ

Large values of the deflection of the vertical ($\sim 50$ $\mu$ rad = 10 s of arc) occur along the Udintsev FZ because of its large age offset ($\sim 18$ Ma, *Weissel et al.* [1977]). Examples of along-track deflection of the vertical profiles, computed by differentiating a subset of descending Seasat altimeter passes, are shown in Figure 7. These are plotted on an oblique Mercator projection where the pole is the relative rotation axis between the Antarctic and Pacific plates (64.67°N, 279.77°E, *Minster and Jordan* [1978]). On this projection the Heezen, Tharp, and Udintsev transform faults are heavy horizontal lines (Figure 7), whereas segments of the Pacific-Antarctic spreading ridge are vertical heavy lines. On the Pacific plate (i.e., left of the heavy line), positive deflection values near the Udintsev FZ are filled, since the age offset is positive when looking from north to south. Similarly, negative peak values are filled on the Antarctic plate because the age offset is negative there. Although deflections of the vertical are larger along the Eltanin FZ system, they are difficult to interpret because the Heezen and Tharp FZ's are so close together.

Deflections of the vertical along the Udintsev FZ show a simple systematic pattern. At the midpoint between the two spreading ridges, a positive peak lies to the north of the transform fault, while a negative peak lies to the south. At the left ridge-transform intersection there is only a positive peak. Further to the left, along the inactive portion of the FZ, there is a positive peak centered above the FZ with a negative sidelobe on the older side. An analogous pattern occurs along the right inactive FZ segment. Thus along all inactive portions of the Udintsev FZ there is a prominent sidelobe on the older side with a small or absent sidelobe on the younger side.

Two features of the deflection profiles across the Udintsev FZ support the model which includes the elastic layer. The first is the persistence of the deflection of the vertical signature along older portions of the Udintsev FZ. This signal persists to at least 60 Ma, where it diminishes because of a decrease in age offset (J. Weissel, personal communication, 1983). The second confirmation of the flexure model is the apparent asymmetry in deflection of the vertical.

TABLE 1. Definitions and Values of Parameters

| Parameter | Definition | Value/Units |
|---|---|---|
| $\alpha$ | thermal expansion coefficient | $3.1 \times 10^{-5}$ K$^{-1}$ |
| $d_{ref}$ | ridge crest depth | 2500 m |
| $E$ | Young's modulus | $6.5 \times 10^{10}$ Pa |
| $g$ | acceleration of gravity | 9.82 m s$^{-2}$ |
| $G$ | gravitational constant | $6.67 \times 10^{-11}$ Nm$^2$ kg$^{-2}$ |
| $\kappa$ | thermal diffusivity | $8 \times 10^{-7}$ m$^2$ s$^{-1}$ |
| $\nu$ | Poisson's ratio | 0.25 |
| $\rho_m$ | mantle density | 3330 kg m$^{-3}$ |
| $\rho_w$ | seawater density | 1025 kg m$^{-3}$ |
| $T_c$ | stress relaxation temperature | 450°C |
| $T_m$ | mantle temperature | 1365°C |
| $T_s$ | surface temperature | 0°C |

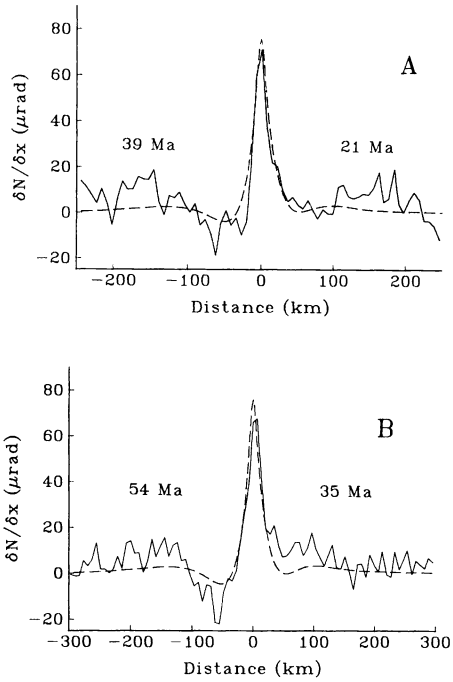


Fig. 8. Deflection of the vertical profiles across the Udintsev FZ (solid curves). Predictions of thermomechanical model (dashed curves). Locations of profiles A and B are shown in Figure 7.

Quantitative agreements between model profiles and observed profiles are shown in Figure 8. The locations of the two profiles are marked in Figure 7. Profile A was inverted and replotted (solid curve) along with the model prediction (dashed curve). For all profiles, no attempt was made to improve the fit by adjusting model parameters. The zero level of the data was, however, adjusted to account for regional trends in the geoid. For both profiles the model matches the data fairly well, although there are short-wavelength variations in the data that cannot be fit by the model. The model agrees equally well with about half of the other profiles shown in Figure 7. Disagreements of the model with the other profiles could be due to crustal thickness variations or deviations of the thermal structure from the boundary layer cooling model.

## THE ROMANCHE FZ

The Romanche FZ in the Equatorial Atlantic is a major age offset ($\sim 40$ Ma, *Sclater et al.* [1980]) resulting from the jagged rifting of South America and Africa [*Wilson*, 1965]. This major FZ, like other smaller age-offset FZ's in the Atlantic, does not have the simple ridge and trough flexural topography that is characteristic of Pacific FZ's. Altantic FZ's either slip to relieve stresses produced by differential subsidence or their flexural signal ($\sim 1$ km) is masked by other large-amplitude topography [*Sandwell and Schubert*, 1982*b*]. Unlike Pacific FZ's, Atlantic FZ's generally consist of a narrow deep central valley surrounded by bordering ridges [*Van Andel et al.*, 1971]. For example, *Bonatti et al.* [1977] demonstrated that the northern wall of the Romanche FZ was near or possibly above sea level during the late Cenozoic. This amplitude is much greater than the prediction of *Sandwell and Schubert*'s [1982*b*] model. Moreover, the ridge is on the older lithosphere rather than the younger lithosphere as predicted by their

model. These extreme variations in seafloor topography are perhaps caused by stresses within the active transform fault and may reflect variations in crustal thickness [*Detrick and Purdy*, 1980]. Despite the failure of the model to explain the rugged topography of Atlantic FZ's, the FZ flexure model seems to explain the gravity field reasonably well.

Examples of ascending Seasat profiles across the Romanche FZ are shown in Figure 9. The heavy black line marks the boundary between the South American and African plates. It consists of spreading ridge segments offset by transform faults. The largest offset occurs at the Romanche transform fault. These 80 along-track deflection of the vertical profiles have the same characteristic signatures as the Udintsev FZ profiles. The profiles crossing the western segment of the FZ have positive deflections of the vertical reflecting the decrease in age from south to north across the FZ. There are negative sidelobes on the south side (i.e., older side). Analogous signatures occur along the eastern segment of the Romanche FZ. Within the transform fault the profiles are very complicated but show the same characteristics as the profiles across the Udintsev transform fault.

Quantitative model comparisons are shown in Figure 10. Locations of these two profiles are marked on Figure 9. Considering the complex topography of this area, the agreements are good. For both profiles the model (dashed curves) overpredicts the peak values of deflection. The disagreement is greater for profile B, which crosses the FZ at an average age of 55 Ma. For comparison the model with no elastic layer is shown as the dotted curve in Figure 10. This curve, which represents the thermal contribution to the geoid signature, is too wide and short to match the observed profile. The fit to profile B is better when the elastic layer is included. The disagreement directly above the FZ could be due to a number of factors, including (1) unmodeled variations in crustal thickness, (2) partial slip along the FZ, (3) lower lithosphere temperature deviations from the boundary layer cooling model, or (4) incorrect estimates of age offset along the older portion of the FZ. Seafloor ages could be incorrect because there are no identified magnetic anomalies in this equatorial area. It is likely that the St. Paul FZ, which is 220 km to the north of the Romanche FZ, has a greater age offset than shown in *Sclater et al.* [1980], while the Romanche FZ has a smaller age offset than reported.

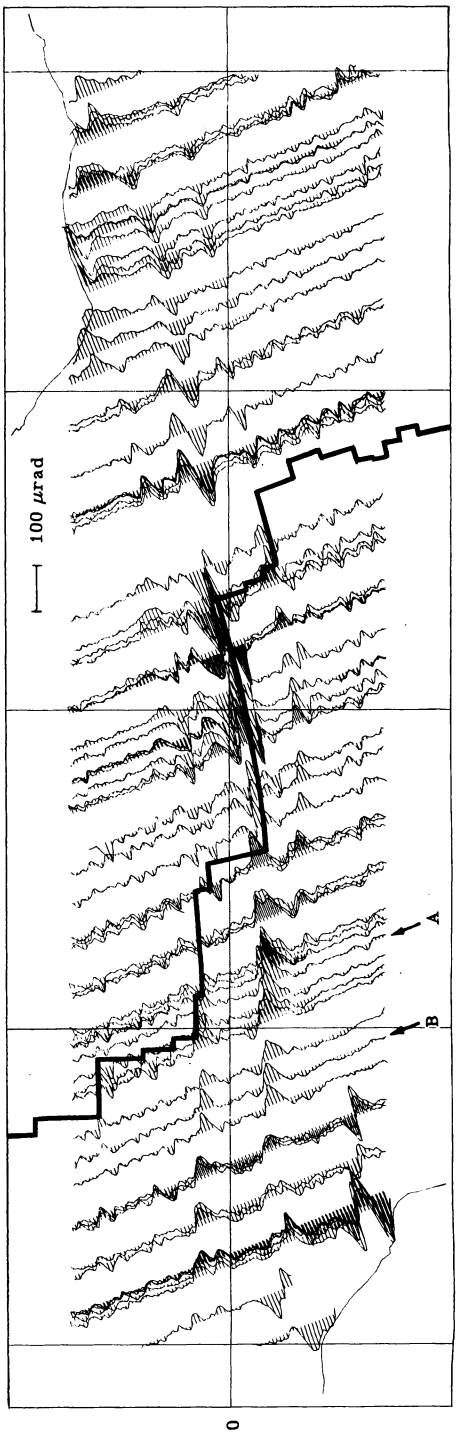


Fig. 9. Along-track deflection of the vertical profiles across Atlantic equatorial FZ's. Heavy line marks the boundary between the South American and the African plates. The largest offset is the Romanche transform fault.

## THE MENDOCINO FZ

Figure 11 shows many deflections of the vertical profiles across the Mendocino FZ in the Northeast Pacific. Geoid profiles over this FZ have been studied by a number of investigators [*Crough*, 1979; *Detrick*, 1981; *Sandwell and Schubert*, 1982*a*; *Cazenave et al.*, 1982]. While these investigators successfully interpreted the overall geoid step as a thermogravitational edge effect, none was able to explain the shape of the step. The most systematic unexplained feature of the geoid profiles was the depression on the older side of the FZ. This corresponds to the negative sidelobe on deflection of the vertical profiles. The FZ model incorporating the elastic layer is able to explain the negative sidelobe as well as the other main characteristics of the deflection profiles across the Mendocino FZ. Three examples are shown in Figure 12. Locations of these profiles are shown in Figure 11.

It is remarkable that this model is able to match the data along the older portions of this FZ (e.g., profile C in Figure 12). The plate cooling model, which explains the North Pacific

depth-age relation [*Parsons and Sclater*, 1977], predicts that the thermal portion of the FZ geoid step will decrease by a factor of 2 when the average age of the lithosphere is 90 Ma. If such a decrease does occur, it does not significantly alter the deflection of the vertical because the flexural portion of the signal is much greater than the thermal portion. This insensitivity of the deflection of the vertical to the thermogravitational edge effect suggests that estimates of geoid offset across FZ's should be made using geoid profiles rather than their derivative. There are problems, however, with estimating geoid offsets directly from geoid profiles. These are discussed in the following section.

## Discussion

In a number of recent studies [*Crough*, 1979; *Detrick*, 1981; *Sandwell and Schubert*, 1982*a*; *Cazenave et al.*, 1982] the relationship between geoid height and seafloor age was extracted from geoid profiles across large age-offset FZ's. In each study the overall amplitude of the geoid step was estimated either visually or by fitting a simple model to the observations. The step amplitude was then normalized by the age offset and plotted as a function of age. When analyzed in this manner, the data are easily compared with prediction of lithosphere cooling models. The overall amplitudes of the geoid steps are, however, difficult to estimate because their shapes are not well understood and they are superimposed upon regional trends that are unrelated to FZ's. Models of geoid steps presented here agree with the shapes of observed geoid steps and therefore provide a basis for estimating amplitudes of geoid steps. Detrick, using the boundary layer cooling model with no flexure or lateral heat conduction, showed that realistic procedures for estimating FZ geoid offsets will always underestimate their amplitude. At the ridge-transform intersection his model predicted a sharp geoid step so underestimation is minimal. When the average age of the lithosphere reaches 80 Ma, however, the step estimation method proposed by Crough underestimates the total offset by 25%. Detrick accounted for this bias when interpreting his geoid offset data across the Mendocino FZ.

In this study, *Detrick*'s [1981] analysis for determining the step estimation bias is performed on the thermomechanical model developed above. An example is shown in Figure 13, where two model geoid height profiles are plotted. The solid curve is the geoid step across a FZ separating lithosphere of ages 20 Ma (left) and 0 Ma (right). The dashed curve is the model prediction after the FZ has aged by 80 Ma. These steps were estimated by visually fitting straight lines to the profiles; data within 100 km of the FZ are excluded from the fitting process. These lines were extrapolated back to zero to determine the estimated offset. The predicted offset is the desired quantity. For this case it has a value of 3.02 m. Estimated offsets are 2.70 m and 1.56 m for the solid and dashed profiles, respectively. For the solid curve the ratio of estimated offset to predicted offset is 0.89. This agrees with Detrick's result. The same ratio for the dashed curve is 0.52, which is substantially less than Detrick's value of 0.75. The difference is due to lithospheric flexure and lateral heat conduction.

The same experiment was performed on FZ's with 10 Ma and 30 Ma age offsets; the results are similar when the ratio of estimated offset to predicted offset is plotted against the average age of the two lithospheric segments. (Note: *Detrick*'s [1981] bias model is also independent of age offset when plotted against average age rather than time in contact.) The results are summarized in Figure 14. The dashed curve is Detrick's bias model, and the solid curve is the bias model developed here. If the thermomechanical FZ model is correct, then reasonable methods for measuring geoid offset will underestimate the total offset by 20% at 20 Ma and 40% at 50 Ma. This underestimation, if not accounted for, will lead to false conclusions about the growth of the thermal boundary layer.

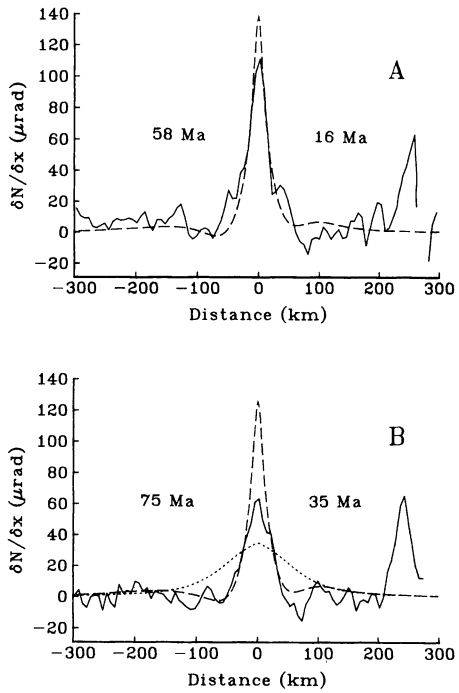


Fig. 10. Two profiles across the Romanche FZ (solid curves). Locations are shown in Figure 9. Dashed curves are predictions of the thermomechanical model. Dotted curve is prediction of the model with no elastic layer. The St. Paul FZ lies 220 km to the north.

Depth versus age data are best fit by a plate cooling model with an asymptotic thickness of 110 to 140 km. This same model predicts that the geoid height versus age relation will begin to flatten (i.e., deviate from the boundary layer cooling model prediction) at about 40 Ma. Geoid slope versus age data which are biased by the step estimation procedure will show an additional flattening beginning at about 20 Ma. Very thin lithospheres must be used to fit biased geoid slope versus age data. Unfortunately, interpretation of geoid age relations derived from FZ geoid profiles will vary among investigators, depending upon their understanding of the shape of geoid steps. The method used by *Sandwell and Schubert* [1982*a*] does not suffer from this problem, since it uses the deflection of the vertical. However, it was shown in the previous section that deflections of the vertical across old FZ's are insensitive to the thermogravitational edge effect so their results may not be as accurate as reported. This is especially true for ages greater than 60 Ma.

The agreements between the model predictions and the deflections of the vertical along major FZ's as well as bathymetric profiles across the Mendocino FZ [*Sandwell and Schubert*, 1982*b*] are direct evidence that FZ's are not zones of weakness. They have been interpreted as weak zones in the lithosphere because of their fractured seafloor and their slightly higher than normal [*Bergman and Solomon*, 1980] or normal seismicity [*Okal et al.*, 1980]. This possibly higher

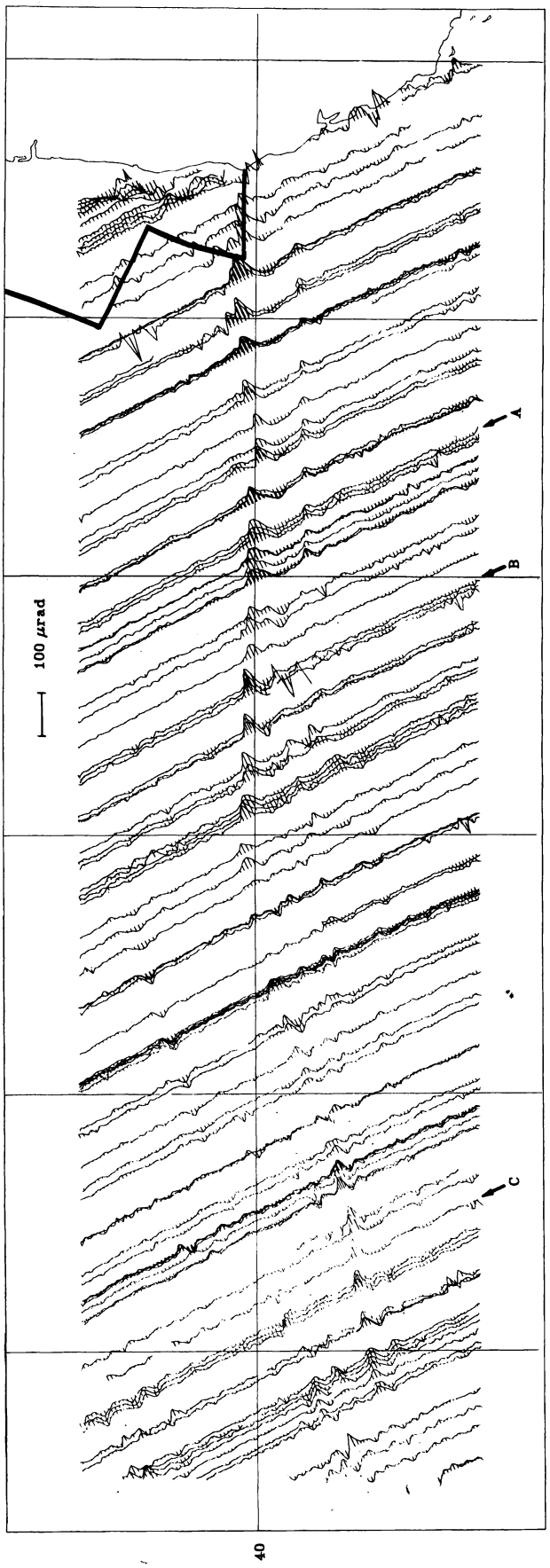


Fig. 11. Along-track deflection of the vertical profile across the Mendocino FZ. The smaller Pioneer FZ lies to the south. The heavy line marks the plate boundary. Between longitudes of 200° and 215°, the Mendocino FZ shows the leaky transform pattern [*Menard and Atwater*, 1969].

seismic activity may reflect the higher than normal stresses near a FZ rather that FZ weakness. The sensitivity of the flexure signature to the initial conditions indicates that the older and younger segments of lithosphere become welded together within the first couple million years beyond the ridge-transform intersection. It is interesting that the mechanical bond is not disrupted by thermoelastic stresses within the elastic layer, especially those stresses produced by differential contraction along the strike of the FZ. It is possible that shear stresses for very large age-offset FZ's (>25 Ma) may exceed the strength of the lithosphere, resulting in catastrophic failure and magma leakage. Indeed, the FZ's with very large age offsets lie beneath the Ninetyeast Ridge and the Louisville Ridge. The proximity of these two ridges to large age offsets in the lithosphere may not be coincidental. Recent evidence along the Louisville Ridge [*Watts and Ribe*, this issue] indicates that the ridge formed after the FZ. One must conclude that the FZ is responsible for the Louisville Ridge. It is likely that it formed by catastrophic failure of the FZ. The results of this study suggest that even if failure did occur along a major FZ it is not a sign of FZ weakness. Rather the FZ is a zone of high thermomechanical stress.

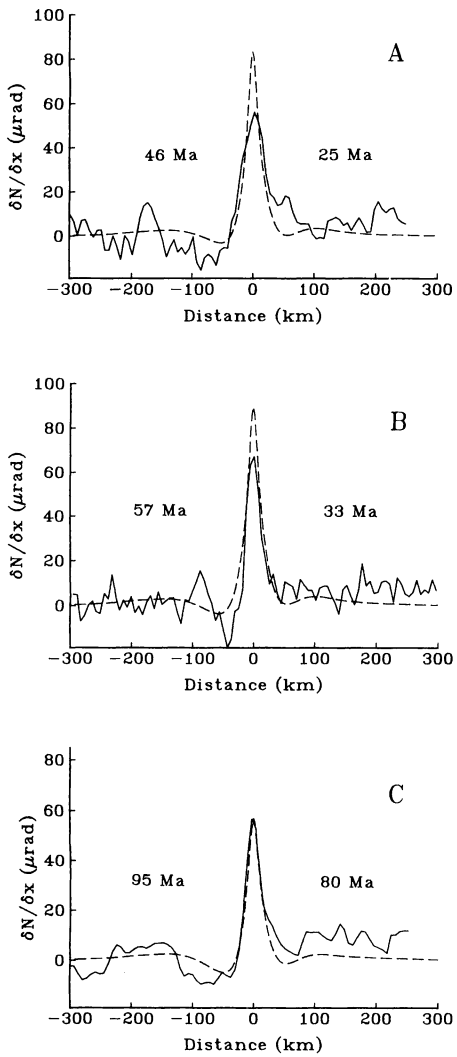


Fig. 12. Three profiles across the Mendocino FZ (see locations in Figure 11). The model matches profile C, which crosses the older (90-Ma) part of the FZ.

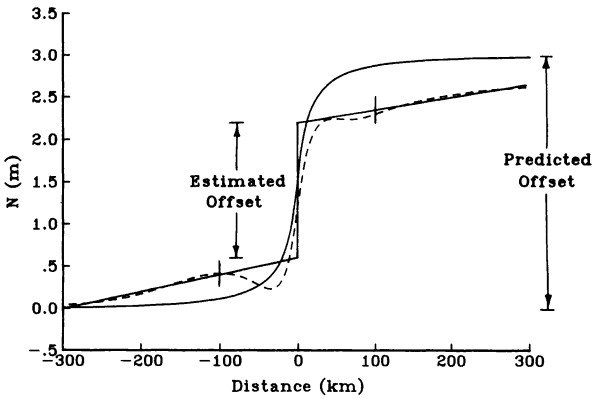


Fig. 13. Comparison between estimated offset and predicted offset for a FZ with a 20-Ma age offset. The age of the right side is 0 Ma for the solid curve and 80 Ma for the dashed curve. The ratio of estimated offset to predicted offset is 0.89 for the young FZ (solid curve) and 0.52 for the older FZ (dashed curve).

## SUMMARY

1. Large age-offset oceanic FZ's display a number of topographic and gravitational characteristics. These include ridges on the younger lithospheric plate and troughs on the older lithospheric plate which persist on old seafloor as well as a sharp gravitational edge effect which is asymmetric across the FZ and also persists on very old seafloor.

2. These characteristics cannot be explained by a thermal conduction model where the lithosphere is in local isostatic equilibrium. The local compensation model predicts that topography, deflection of the vertical, and free-air gravity signatures across FZ's will become increasingly smooth and ultimately disappear as the FZ ages. These topographic and gravitational characteristics are explained, however, by a thermal conduction model incorporating a continuous elastic layer where the base of the elastic layer is defined by the stress relaxation temperature $T_e$. Since the elastic layer varies in thickness across the FZ, a rapid numerical technique was developed for calculating the flexural response of the lithosphere to space and time-dependent thermal buoyancy forces. Because of the continuity of the elastic layer, the scarp, formed at the ridge-transform intersection, remains constant with age. This frozen-in scarp, along with the difference in subsidence rates far on either side of the FZ, results in the characteristic ridge and trough topography.

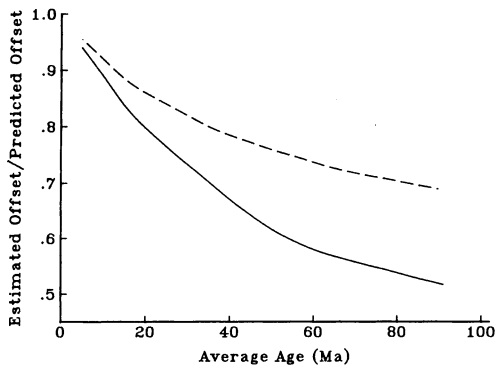


Fig. 14. Bias in estimating geoid offset (i.e., estimated offset/predicted offset) versus the average age of the lithosphere across the FZ. Dashed curve is bias for FZ model with no elastic layer [after *Detrick*, 1981]. Solid curve is bias for model with elastic layer. At 80 Ma, geoid offsets may be underestimated by 50%.

3. Modeling results are extremely sensitive to the initial thermal structure at the ridge-transform intersection. More accurate initial conditions await a complete thermomechanical description of the active transform fault. This active segment contains systematic topographic and gravitational characteristics that will help constrain models.

4. If the model is correct, then most techniques for estimating geoid offsets across FZ's will substantially underestimate their true offset. This estimation bias, if not accounted for, makes the thermal boundary layer appear thin.

## APPENDIX: FLEXURE WITH VARIABLE RIGIDITY

The differential equation describing two-dimensional flexure of a thin elastic plate of density $(\rho_m - \rho_m)$ overlying a fluid half space and subject to a uniform gravitational acceleration $g$ is

$$\frac{d^2}{dx^2}\left(D(x)\frac{d^2w(x)}{dx^2}\right) + \bar{g}(\rho_m - \rho_w)w(x) = P(x) \tag{A1}$$

where $D(x)$ is the spatially variable flexural rigidity, $w(x)$ is the deflection of the plate, and $P(x)$ is the applied load. The boundary conditions are

$$\lim_{|x|\to\infty} w(x) = 0 \tag{A2}$$

and

$$\lim_{|x|\to\infty} \frac{dw(x)}{dx} = 0$$

It is assumed that $D$, $w$, and $P$ are band-limited function so their Fourier transforms exist. Forward and inverse Fourier transforms are defined in equations (10) and (11), respectively.

The functions $D$ and $w$ can be written as

$$D(x) = \frac{1}{2\pi}\int_{-\infty}^{\infty} \hat{D}(s)e^{isx}\,ds \tag{A3}$$

$$w(x) = \frac{1}{2\pi}\int_{-\infty}^{\infty} \hat{w}(r)e^{irx}\,dr \tag{A4}$$

Upon substituting these expressions for $D$ and $w$ into the first term of (A1) and differentiating under the integral, the following is obtained

$$\frac{1}{(2\pi)^2}\int_{-\infty}^{\infty}\int_{-\infty}^{\infty}(r+s)^2r^2\hat{D}(s)\hat{w}(r)e^{i(s+r)x}\,dr\,ds + \bar{g}(\rho_m - \rho_w)w(x) = P(x) \tag{A5}$$

Fourier transformation of (A5) yields

$$\frac{1}{(2\pi)^2}\int_{-\infty}^{\infty}\int_{-\infty}^{\infty}(r+s)^2r^2\hat{D}(s)\hat{w}(r)\int_{-\infty}^{\infty}e^{i(s+r-k)x}\,dx\,dr\,ds + \bar{g}(\rho_m - \rho_w)\hat{w}(k) = \hat{P}(k) \tag{A6}$$

By making use of the fact that

$$\frac{1}{2\pi}\int_{-\infty}^{\infty} e^{i(s+r-k)x}\,dx = \delta[r - (k-s)] \tag{A7}$$

performing the integral with respect to $r$, and using the band-limited property of $\hat{D}(s)$ (i.e., $\hat{D}(s) = 0$, $|s| > \beta$); (A6) is reduced to a Fredholm integral equation

$$\frac{k^2}{2\pi}\int_{-\beta}^{\beta}\hat{D}(s)\hat{w}(k-s)(k-s)^2\,ds + \bar{g}(\rho_m - \rho_w)\hat{w}(k) = \hat{P}(k) \tag{A8}$$

Notice that if $D(x) = D_0$ then $\hat{D}(s) = 2\pi D_0\delta(s)$. For this case (i.e., constant flexural rigidity) the solution for $w(k)$ is

$$\hat{w}(k) = [D_0k^4 + \bar{g}(\rho_m - \rho_w)]^{-1}\hat{P}(k) \tag{A9}$$

Let

$$\hat{D}(s) = \hat{D}'(s) + 2\pi D_0\delta(s) \tag{A10}$$

Inserting (A10) to (A8), integrating and rearranging terms yields

$$\hat{w}(k) = [D_0k^4 + \bar{g}(\rho_m - \rho_w)]^{-1}\cdot\left[\hat{P}(k) - \frac{k^2}{2\pi}\int_{-\beta}^{\beta}\hat{D}'(s)\hat{w}(k-s)(k-s)^2\,ds\right] \tag{A11}$$

Equation (A11) can be rewritten as

$$\hat{w}(k) = T[\hat{w}(k)] \tag{A12}$$

where $T$ is a linear operator.

If $T$ is a continuous contraction operater over a complete metric space, then (A12) can be solved by successive approximation [*Korevaar*, 1968]. The successive approximation method consists of making an initial guess at the solution, $w_0$ (e.g., zero is a good guess). The operation $T[w_0]$ results in a closer approximation to the true solution. This procedure is repeated (e.g., $w_i = T[w_{i-1}]$) until the desired numerical accuracy is achieved. The sequence $w_0, w_1, w_2, \ldots$ is Cauchy (i.e., $d(w_j, w_l)\to 0$ as $j$ and $l$ tend to $\infty$, $d(\ ,\ )$ is the norm), and it converges uniformly to the true solution. In practice the convolution integral in (A11) should be evaluated by using the convolution theorem along with a FFT routine. This numerical approach saves not only computer and programming time, but it is also more accurate.

Whether or not this scheme converges, the rate of convergence is governed by the properties of $T$ and therefore $D$. $T$ is a contraction operator if there exists a positive constant $r < 1$ such that

$$d(T[\hat{X}], T[\hat{Y}]) \le rd(\hat{X}, \hat{Y}) \tag{A13}$$

where $\hat{X}(k)$ and $\hat{Y}(k)$ lie in the metric space. The rate of convergence is high for small positive values of $r$ and becomes lower as $r$ approaches 1. For the Fredholm integral equation the infinity norm $L_\infty$ is used to test for the contraction property of $T$

$$d(\hat{X}, \hat{Y}) = \max_{-\infty<k<\infty}|\hat{X} - \hat{Y}| \tag{A14}$$

Inserting (A11) into (A13) yields

$$\max_{-\infty<|k|<\infty}\left|\frac{k^2}{2\pi[D_0k^4 + \bar{g}(\rho_m - \rho_w)]}\cdot\int_{-\beta}^{\beta}\hat{D}'(s)(k-s)^2[\hat{X}(k-s) - \hat{Y}(k-s)]\,ds\right| < \max_{-\infty<k<\infty}|\hat{X}(k) - \hat{Y}(k)| \tag{A15}$$

However, the left side of (A15) is less than

$$\max_{-\infty<k<\infty}|\hat{X}(k) - \hat{Y}(k)|\cdot\max_{-\infty<k<\infty}\left|\frac{k^2\int_{-\beta}^{\beta}\hat{D}'(s)(k-s)^2\,ds}{2\pi[D_0k^4 + \bar{g}(\rho_m - \rho_w)]}\right|$$

so if (A15) is true, the following must also be true for all values of $k$:

$$\int_{-\beta}^{\beta}\hat{D}'(s)k^2(k-s)^2\,ds < 2\pi[D_0k^4 + \bar{g}(\rho_m - \rho_w)] \tag{A16}$$

The condition given in (A16) ensures that the iteration scheme

converges and it should be tested in the portion of the wave number spectrum being considered for a particular problem.

*Acknowledgments.* I thank Jerry Schubert for the ideas he contributed during the early stages if this research. A portion of this work was supported by the NASA Geodynamics Program under grant NAG 5152.

## REFERENCES

Bergman, E. A., and S. C. Solomon, Oceanic intraplate earthquakes: Implications for local and regional intraplate stress, *J. Geophys. Res.*, *85*, 5389–5410, 1980.

Beyer, W. H., *CRC Standard Mathematical Tables*, 24th ed., CRC Press, Cleveland, Ohio, 1976.

Bonatti, E., M. Sarnthein, A. Boersma, M. Gorini, and J. Honnorez, Neogene crustal emersion and subsidence at the Romanche fracture zone, Equatorial Atlantic, *Earth Planet. Sci. Lett.*, *35*, 369–383, 1977.

Born, G. H., J. A. Dunne, and D. B. Lame, SEASAT mission overview, *Science*, *204*, 1405–1406, 1979.

Caldwell, J. G., and D. L. Turcotte, Dependence of the thickness of the elastic oceanic lithosphere on age, *J. Geophys. Res.*, *83*, 7572–7579, 1979.

Carslaw, H. S., and J. C. Jaeger, *Conduction of Heat in Solids*, 2nd ed., Oxford University Press, New York, 1959.

Cazenave, A., B. Lago, and K. Dominh, Geoid anomalies over the northeast Pacific fracture zones from satellite altimeter data, *Geophys. J. R. Astron. Soc.*, *69*, 15–31, 1982.

Crough, S. T., Geoid anomalies across fracture zones and the thickness of the lithosphere, *Earth Planet. Sci. Lett.*, *44*, 224–230, 1979.

Detrick, R. S., Jr., An analysis of geoid anomalies across the Mendocino fracture zone: Implications for thermal models of the lithosphere, *J. Geophys. Res.*, *86*, 11,751–11,762, 1981.

Detrick, R. S., and G. M. Purdy, The crustal structure of the Kane fracture zone from seismic refraction studies, *J. Geophys. Res.*, *85*, 3759–3777, 1980.

Forsyth, D. W., and B. Wilson, Three-dimensional temperature structure of a ridge-transform-ridge system, *Earth Planet. Sci. Lett.*, in press, 1984.

Korevaar, J., *Mathematical Methods*, vol. 1, p. 215, Academic, New York, 1968.

Louden, K. E., and D. W. Forsyth, Thermal conduction across fracture zones and the gravitational edge effect, *J. Geophys. Res.*, *81*, 4869–4874, 1976.

Menard, H. W., and T. Atwater, Origin of fracture zone topography, *Nature*, *222*, 1037–1040, 1969.

Minster, J. B., and T. H. Jordan, Present-day plate motions, *J. Geophys. Res.*, *83*, 1978.

Okal, E. A., J. J. Talandier, K. A. Sverdrup, and T. H. Jordan, Seismicity and tectonic stress in the South Central Pacific, *J. Geophys. Res.*, *85*, 6479–6495, 1980.

Parker, R. L., The rapid calculation of potential anomalies, *Geophys. J. R. Astron. Soc.*, *31*, 447–455, 1972.

Parker, R. L., and D. W. Oldenburg, Thermal model of ocean ridges, *Nature Phys. Sci.*, *242*, 137–139, 1973.

Parsons, B., and J. G. Sclater, An analysis of the variation of ocean floor bathymetry and heat flow with age, *J. Geophys. Res.*, *82*, 803–827, 1977.

Sandwell, D. T., and G. Schubert, Geoid height-age relation from Seasat altimeter profiles across the Mendocino fracture zone, *J. Geophys. Res.*, *87*, 3949–3958, 1982a.

Sandwell, D. T., and G. Schubert, Lithospheric flexure at fracture zones, *J. Geophys. Res.*, *87*, 4657–4667, 1982b.

Sclater, J. G., C. Jaupart, and D. Galson, The heat flow through oceanic and continental crust and the heat loss of the earth, *Rev. Geophys. Space Phys.*, *18*, 269–311, 1980.

Stanley, H. R., The GEOS-3 project, *J. Geophys. Res.*, *84*, 3779–3783, 1979.

Turcotte, D. L., and E. R. Oxburgh, Finite amplitude convective cells and continental drift, *J. Fluid Mech.*, *28*, 24–42, 1967.

Van Andel, T. H., R. P. Von Herzen, and J. D. Phillips, The Vema fracture zone and tectonics of transverse shear zones in oceanic crustal plates, *Mar. Geophys. Res.*, *1*, 261–283, 1971.

Watts, A. B., An analysis of isostasy in the world's oceans, 1, Hawaiian-Emperor seamount chain, *J. Geophys. Res.*, *83*, 5989–6004, 1978.

Watts, A. B., J. H. Bodine, and M. S. Steckler, Observations of flexure and the state of stress in the oceanic lithosphere, *J. Geophys. Res.*, *85*, 6369–6377, 1980.

Watts, A. B., and M. W. Ribe, On geoid heights and flexure of the lithosphere at seamounts, *J. Geophys. Res.*, this issue.

Weissel, J. K., D. E. Hayes, and E. M. Herron, Plate tectonics synthesis: The displacements between Australia, New Zealand, and Antarctica since the late Cretaceous, *Mar. Geol.*, *25*, 231–277, 1977.

Wilson, J. T., A new class of faults and their bearing on continental drift, *Nature*, *207*, 343–347, 1965.

D. T. Sandwell, National Geodetic Survey, Charting and Geodetic Services, National Ocean Service, National Oceanic and Atmospheric Administration, Rockville, MD 20852.

(Received January 25, 1984;
revised June 29, 1984;
accepted August 15, 1984.)